Highlights

Efficient quantification of composite spatial variability: A multiscale framework that captures intercorrelation

B. Van Bavel, Y. Zhao, M. G.R. Faes, D. Vandepitte, D. Moens

- Propagation of uncertainty of unidirectional carbon-fibre-reinforced composite plies
- Stochastic fibre misalignment, volume fraction and fibre strength from measurements
- Intercorrelated finite element homogenised properties using vine copula models
- Efficient multiscale methodology accurately predicts unidirectional failure load
- Stochastic fibre misalignment and volume fraction reduce tensile strength considerably

Efficient quantification of composite spatial variability: A multiscale framework that captures intercorrelation

B. Van Bavel[a,*], Y. Zhao[b], M. G.R. Faes[c], D. Vandepitte[a], D. Moens[a]

[a] *KU Leuven, Department of Mechanical Engineering, LMSD, Celestijnenlaan 300, Heverlee, B-3001, Belgium*
[b] *KU Leuven, Department of Metallurgy and Materials Engineering, SCALINT, Celestijnenlaan 300, Heverlee, B-3001, Belgium*
[c] *TU Dortmund University, Chair for Reliability Engineering, Leonhard-Euler-Straße 5, Dortmund, D-44227, Germany*

Abstract

Composite structures suffer from material imperfections. Non-deterministic models at the micro- and mesoscale propagate this spatial variability. However, they become impractical when the structure size increases. This paper proposes a numerically efficient multiscale methodology that links structural behaviour with the spatial variability of material imperfections on smaller scales. Fibre strength variability is accounted for through a fibre break model. A mesoscale model considers fibre volume fraction and fibre misalignment variability using random fields. Measurements provide probabilistic data for these imperfections. Subsequent homogenisation results in intercorrelated material properties on the structural macroscale that are modelled effectively with vine copulas. The methodology is verified by predicting the failure load of a coupon model. Predictions are very similar to those obtained by directly modelling spatial variability on the structural scale.

Keywords: Multiscale, Reliability analysis, Finite element analysis (FEA), Spatial variability, Vine copula modelling, Unidirectional (UD), Carbon-fibre-reinforced polymers (CFRP), Strength prediction

1. Introduction

Carbon fibres have a very high intrinsic strength of well over 20 GPa [1]. A simple rule of mixtures would suggest a similar value for unidirectional *carbon-fibre-reinforced polymers* (CFRPs). In practice, however, the strength is considerably lower than this value, often not exceeding a few GPa. It behaves more stochastically as well [2].

Material imperfections explain this difference to a large extent. Fibre surface defects, among other imperfections, lead to a stochastic fibre strength commonly modelled by a Weibull distribution [3]. In combination with, for example, misaligned fibres [4–6], unevenly distributed [2] fibres or voids [7] in the matrix material this affects the stochastic behaviour of composite structures.

The effect of such imperfections on the microscale behaviour has been studied extensively. Fibre break models account for fibre strength stochasticity [2], and microscale *finite element* (FE) homogenisation often accounts for inhomogeneous fibre distributions [8]. In structural simulations, however, propagation of material variability remains challenging. Stochastic composite tube or pressure vessel analyses in literature generally disregard spatial variability [9–16]. Instead, a single stochastic variable models the longitudinal stiffness E_{11} of a single layer of the laminate [15], sometimes without substantiating its stochastic input parameters. While other studies account for spatial variability, they ignore the spatial correlation between material properties of adjacent elements. Likewise, intercorrelation between material properties is neglected [17–22].

Garcia-Martin et al. [17] introduce intralayer variability of the Young's modulus and Poisson coefficient in their material, using data obtained from DIC measurements. However, both the inter- and autocorrelation structure of these variables are not considered. Malgioglio et al. [6] include spatial variability by modelling the fibre misalignment and fibre volume fraction as random fields. The small correlation lengths of these imperfections, however, result in a prohibitively small element size (tens of µm) in the FE analysis, limiting its use in large structural analyses.

Prior research by Van Bavel et al. [23] alleviates this problem by providing a multiscale framework. A mesoscale model implements spatial variability. The macromodel, on its turn, retrieves effective material properties by homogenizing the mesomodel. Therefore, it remains computationally inexpensive, while the intercorrelation between the resulting effective material properties is modelled with a vine copula model. This efficiency enables new insights on the effect of individual material imperfections on the output stochasticity. Moreover, the research identifies that mesoscale boundary conditions significantly affect the calculated effective strength.

This paper improves the multiscale framework and focuses on mesoscale variability. The proposed methodology

*Corresponding author at: KU Leuven, Department of Mechanical Engineering, LMSD, Celestijnenlaan 300, B-3001 Heverlee, Belgium

Email address: ben.vanbavel@kuleuven.be (B. Van Bavel)

Nomenclature

A	Surface area in hierarchical scaling law
B	Body considered for homogenisation
∂B	Boundary of body B
C	Covariance function; Copula; Stiffness matrix
E_{ii}	Young's modulus along axis i
E_D	Strain energy density
F	Cumulative distribution function
G_{ij}	Shear modulus in direction j on the plane with normal direction i
I	Fibre bundle level
S	Compliance matrix
V_f	Fibre volume fraction
X	Gaussian random field
$\hat{X}$	Discretized Gaussian random field
Y	Non-Gaussian random field
Y_{11}	Thermodynamic force
Y_{11}^{lim+}	Longitudinal tensile energy threshold
d	Euclidean distance
d_f	Damage variable
f	Probability distribution function
g	A nonlinear function describing a non-Gaussian distribution in terms of a Gaussian distribution.
l	Correlation length
l_0	Gauge length in fibre strength distribution
m	Weibull modulus in fibre strength distribution
$\boldsymbol{n}$	Outward pointing normal vector
n_f	Number of fibres
p	Non-negative integer in Whittle-Matérn kernel
$\mathbf{s}$	Position in Euclidean space
$\boldsymbol{t}$	Traction vector
$\boldsymbol{u}$	Displacement vector
x	Random variable
ε	Strain
$\boldsymbol{\varepsilon}$	Strain tensor
θ	in-plane (ip) or out-of-plane (op) misalignment angle
λ_i	Eigenvalue i
μ	Arithmetic mean
ν_{ij}	Poisson's ratio corresponding to a contraction in direction j when extending direction i
ξ	Independent standard normal variable
ρ	Autocorrelation function
σ	Stress; Standard deviation
$\boldsymbol{\sigma}$	Stress tensor
σ_{11}	Longitudinal tensile strength
σ_0	Scale parameter in fibre strength distribution
τ_{IL}	Matrix interlaminar shear strength
Φ	Joint Gaussian probability density function
ϕ_i	Eigenvector i
ϕ_f	Fibre diameter
ω	State index of random field evaluation

efficiently and accurately propagates uncertain material imperfections to the structural macroscale. Specifically, fibre misalignment, fibre volume fraction and fibre strength variability are considered. These quantities have a significant impact on the behaviour of composite structures, as illustrated numerously [2, 4–6, 8] and their probabilistic data is relatively well reported [24–26]. This paper is organized as follows. Section 2 elaborates on the introduction of spatial variability into the FE model. Mesoscale random fields model the fibre misalignment and volume fraction variability. In addition, a fibre break model accounts for fibre strength variability. Section 3 presents the multiscale framework. It connects mesoscale spatial variability and macroscale variability of intercorrelated effective material properties using FE homogenisation and vine copula modelling. Section 4 discusses the results and verifies the methodology. It uses a unidirectional composite coupon subjected to a tensile load to compare between directly and indirectly modelling spatial variability on the macroscale. Finally, we draw conclusions in section 5.

2. Spatial variability

This section elaborates on the probabilistic modelling of spatial variability of composite imperfections. First, Section 2.1 presents random fields as a modelling tool for spatially correlated variables. Afterwards, Sections 2.2, 2.3 and 2.4 explain, respectively, the implementation of fibre misalignment, fibre volume fraction and fibre strength variability. As a reference, T700 fibres and an ARALDITE® epoxy are used. Table 1 lists material properties. Measurements made by Mesquita et al. [24] provide data on the strength of T700 fibres.

Fibre elastic properties		Matrix properties [27]		Fibre strength properties [24]	
E_{11} [28]	230 GPa	E	3.15 GPa	Fibre diameter ϕ_f	6.87 µm
$E_{22/33}$ [29]	19 GPa	G	1.21 GPa	Weibull modulus m	3.94 [-]
$\nu_{12/13}$ [29]	0.2 [-]	ν	0.3 [-]	Scale parameter σ_0	4.71 GPa
$G_{12/13}$ [29]	27 GPa	Interlaminar shear strength τ_{IL}	56 MPa	Gauge length l_0	12 mm
G_{23} [29]	7 GPa				

Table 1: Fibre and matrix material properties.

	V_f [%]	θ_{ip} [°]	θ_{op} [°]		l_{ip}^x [µm]	l_{ip}^y [µm]	l_{ip}^z [µm]	l_{op}^x [µm]	l_{op}^y [µm]	l_{op}^z [µm]
Mean	51.67	0.00	0.00	Value	1073	675	71	619	407	339
Standard deviation	4.76	2.23	1.01							

Table 2: Probabilistic data for fibre volume fraction V_f [25] and in-plane θ_{ip} and out-of-plane θ_{op} misalignment, with correlation lengths l_i^j.

2.1. Random fields

Random fields $X(\boldsymbol{s};\omega)$, defined as an indexed set of random variables $x(\omega)$ over some parameter space Ω, can be thought of as a spatial extension of random variables. As a result, sample evaluations do not only depend on the state index ω but also on the evaluated position in space $\boldsymbol{s} \subset \Omega$. Therefore, these random fields provide an excellent tool for modelling spatially correlated composite imperfections, such as the fibre volume fraction at a specific position in the material.

Gaussian random fields can be obtained by a series expansion using some set of convenient functions. Ideally, these form a basis of the Hilbert space $\mathcal{L}^2(\Omega)$ of square integrable functions over Ω. One possible expansion consists of the numerically efficient *Expansion Optimal Linear Estimator* (EOLE) [30]. It uses a spectral decomposition of the autocovariance function $C_{XX}(\boldsymbol{s},\boldsymbol{s}')$ to construct such a basis. The random field representation thus becomes

$$X(\boldsymbol{s};\omega) = \mu(\boldsymbol{s}) + \sum_{i=1}^{\infty} \frac{\xi_i(\omega)}{\sqrt{\lambda_i}} \phi_i^T C_{X(\boldsymbol{s})X}. \tag{1}$$

Herein, $\mu(\boldsymbol{s})$ is the mean of the random field, $\xi_i(\omega)$ are independent standard normal variables, λ_i and ϕ_i are eigenvalues and eigenvectors, respectively, of C_{XX}. Discretization is achieved by truncating the series expansion and evaluating the autocovariance function at a finite number of positions $\{X(\boldsymbol{s}_1), ..., X(\boldsymbol{s}_m)\} \subset \Omega$. In that case C_{XX} becomes an autocovariance matrix.

A stationary random field has a correlation structure that is independent of the position in space. In the assumption of such a stationary field, a simplified Matérn autocorrelation function, written as

$$\rho_{xx} = \exp\left(-\sqrt{2p+1}\bar{d}\right) \frac{p!}{(2p)!} \cdot \sum_{i=0}^{p} \frac{(p+i)!}{i!\,(p-i)!} \left(2\sqrt{2p+1}\bar{d}\right)^{p-i}, \tag{2}$$

provides a versatile analytical fit to many experimental autocorrelations. Here, p is a non-negative integer and $\bar{d}$ a correlation-weighted distance equal to

$$\bar{d} = \sqrt{\left(\frac{d_x}{l_x}\right)^2 + \left(\frac{d_y}{l_y}\right)^2 + \left(\frac{d_z}{l_z}\right)^2}, \tag{3}$$

with d_i the distance between two positions measured along direction i and l_i the correlation length along direction i. The correlation length is defined as the length $l_{0.1}$ for which the autocorrelation becomes smaller than 0.1.

In case of $(p = 0)$ or $(p = \infty)$ this equation simplifies to the popular exponential and squared exponential autocorrelation functions. However, both have important drawbacks, either due to numerical inefficiency (exponential) or lack of physical interpretability (squared exponential). Therefore, $p = 3$ is considered a good compromise [31].

Most random field discretization methods only work with Gaussian fields. A straightforward extension to non-Gaussian fields consists of using the target non-Gaussian *cumulative distribution function* (CDF) $F_Y(\cdot)$ to transform a Gaussian field $X(\boldsymbol{s})$ to its non-Gaussian counterpart $Y(\boldsymbol{s})$, by using

$$Y(\boldsymbol{s}) = F_Y^{-1}\{F_X(X(\boldsymbol{s})), \boldsymbol{s}\} = g(X(\boldsymbol{s}), \boldsymbol{s}), \tag{4}$$

where $F_X(\cdot)$ is the CDF of a standard normal variable. The unknown autocorrelation ρ_{xx} of the underlying Gaussian field is related implicitly to ρ_{yy} by

$$\rho_{yy}\sigma_Y^2 + \mu_Y^2 = \int_{-\infty}^{\infty}\int_{-\infty}^{\infty} g(x_1,\boldsymbol{s})\, g(x_2,\boldsymbol{s})\, \Phi\{x_1, x_2; \rho_{xx}\}\, dx_1 dx_2. \tag{5}$$

The non-Gaussian distribution's mean μ_Y and standard deviation σ_Y are required to normalize the autocorrelation function. Φ is the joint Gaussian probability density function. Equation 5 has to be solved iteratively to find ρ_{xx}, while accounting for the fact that ρ_{xx} might not yield a positive semidefinite autocorrelation matrix [32].

2.2. Fibre misalignment

Mean field image analysis [33] is used to characterize fibre misalignment. This technique measures the average

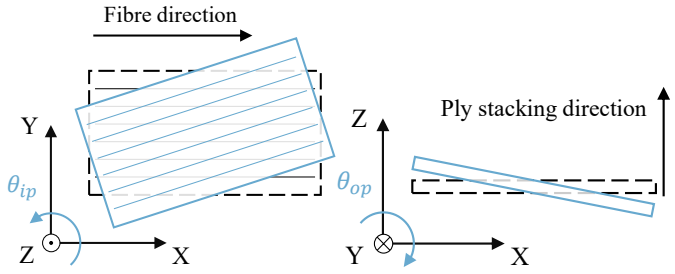

(a) In-plane misalignment (b) Out-of-plane misalignment

Figure 1: Example of θ_{ip} and θ_{op} definition for a schematic UD-ply.

orientation of fibres over a specific area, typically several mm long and wide. Therefore, it is particularly useful for mesoscale implementations where fibres are not modelled explicitly.

The average orientation is decomposed into an in-plane θ_{ip} and out-of-plane θ_{op} misalignment angle. In-plane misalignment is defined as a rotation about the ply stacking direction vector. Out-of-plane misalignment is defined as a rotation about the vector perpendicular to the plane made by the stacking direction vector and the nominal fibre direction vector. Figure 1 illustrates their definition.

The resulting spatially averaged in-plane and out-of-plane misalignment angles are spatially correlated, with correlation lengths on the order of several mm. As an approximation, the fields are stationary and Gaussian [26]. Table 2 lists measured in- and out-of-plane misalignment probabilistic data.

Both misalignment angles are modelled by an independent random field. The local misalignment values are implemented in finite element models by transforming the material coordinate system of the element at the corresponding position. As an illustration, Figure 3 shows both in-plane and out-of-plane misalignment realisations. The random field is calculated for a cuboid unidirectional composite with dimensions $11 \times 7 \times 1.05\,\text{mm}$. Section 3 elaborates on the choice of this model.

2.3. Fibre volume fraction

In contrast to fibre misalignment, the fibre volume fraction V_f does not follow a Normal distribution. Instead, it is left-skewed and better described by a Weibull distribution [25]. Therefore, in this study, a non-Gaussian random field is used to model V_f. Table 2 provides probabilistic data for V_f using measurements from [25].

Sanei and Fertig [25] show that the transverse correlation length of the fibre volume fraction is small, with an uncorrelated window size of only 70 µm. This confirms the observation that most studies involving inhomogeneous transverse fibre distribution in their simulations occur at the microscale [4, 34] rather than at the mesoscale. Moreover, this correlation length determines the transverse element size of the mesomodel as discussed in Section 3. Data on the longitudinal correlation length are not available. As an approximation, the longitudinal correlation length is assumed to be equal to that of θ_{ip}, since determining an exact value is not the focus of this study.

Subsequently, the analytical Mori-Tanaka method [35] is used to derive effective elastic properties from the local fibre volume fraction, rather than a numerical simulation including micro-scale variability since the focus lays on mesoscale variability. Figure 3 shows an example realisation of the fibre volume fraction for the same unidirectional composite used previously for fibre misalignment realisations.

2.4. Fibre strength

The single fibre strength is often modelled by combining the weakest-link theory with a 2-parameter Weibull distribution [36], which yields

$$F_{\sigma_{11}^f}(\sigma) = 1 - \exp\left[-\frac{l}{l_0}\left(\frac{\sigma}{\sigma_0}\right)^m\right]. \tag{6}$$

Equation (6) predicts the failure probability of a single fibre of arbitrary length l at stress σ with Weibull parameters σ_0 and m, fitted at some reference length l_0.

However, it is shown that the (tensile) failure behaviour of composites is more complicated [37]. Fibre breaks cause stress concentrations in neighbouring intact fibres, which now carry a higher load. Therefore, fibre breaks tend to accumulate in clusters. Numerous fibre break models describe this complex failure behaviour. A benchmarking study [2] shows that the analytical model of Pimenta [38] corresponds well with experiments.

This *hierarchical scaling law* (HSL) model considers the failure of fibre bundles of size $n_f = 2^I$. n_f is the number of fibres and I some positive integer indicating the bundle level, as shown in Figure 2. An analytical perfectly plastic shear lag model accounts for stress concentrations around broken fibres. Therefore, failure statistics of a certain bundle level I follow from the failure statistics of the previous bundle level $I-1$, up until the failure strength of a single fibre at $I = 0$. For a specific local fibre volume fraction V_f, the model implicitly assumes that increasing bundle levels have larger cross sections A. Keeping A fixed (corresponding to the element size in FE simulations), the number of fibres n_f (and therefore the bundle level) equals

$$n_f = \frac{4}{\phi_f^2 \pi} A V_f. \tag{7}$$

ϕ_f is the fibre diameter. Generally, the calculated number of fibres does not correspond to an integer valued I. However, its failure distribution can be retrieved by interpolating between the two nearest n_f for which I is integer valued.

After predicting the fibre bundle strength σ_{11}^f with the HSL, a rule of mixtures subsequently calculates the composite tensile strength σ_{11} as

$$\sigma_{11} = \frac{V_f \sigma_{11}^f}{1 - (1 - V_f)\, E^m / E_{11}^f}. \tag{8}$$

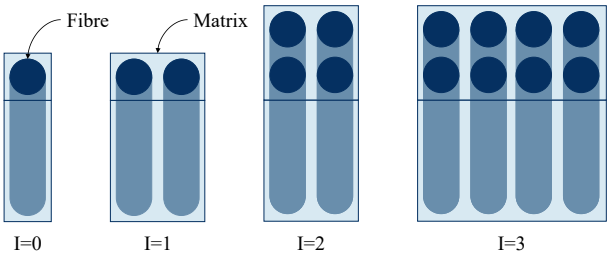

Figure 2: Definition of fibre bundles in the hierarchical scaling law.

It accounts for the matrix E^m and fibre Young's modulus E^f_{11}, assuming matrix and fibre strain are equal. In combination with the previously fixed element size in the HSL, this rule of mixtures results in a correlated fibre volume fraction and composite strength, as shown by Figure 3.

3. Mesoscale model

The next section presents the multiscale framework. Mesoscale imperfections are modelled using the methodology of Section 2. First, Section 3.1 discusses the elastic properties homogenisation of an imperfect mesomodel. Next, Section 3.2 similarly describes tensile strength homogenisation. Finally, Section 3.3 details an intercorrelated model of these homogenised properties using a vine copula.

Both the model and element size of the mesomodel depend on the spatial correlation of the material variability. For the former, the largest correlation lengths determine a minimum model size in order to consider the homogenized properties as variables rather than fields. For the latter, the smallest correlation lengths determine a minimum element size in order to provide a sufficient level of fidelity for the random field modelling, corresponding to roughly 3 to 5 elements per unit of smallest correlation length.

Therefore, the mesomodel is sized $1100 \times 700 \times 350\,\mu\text{m}^3$ in the X-, Y- and Z-directions, respectively. In addition, the element size equals 70 µm in the transverse direction and 110 µm in the longitudinal direction. Figure 4 shows the resulting mesomodel. The figure does not show boundary conditions, since they depend on the FE homogenisation scheme, as explained in the following subsections.

3.1. Elastic properties homogenisation

Homogenisation of elastic properties requires that the Hill condition is satisfied [39]

$$\underbrace{\overline{\boldsymbol{\sigma} : \boldsymbol{\varepsilon}}}_{\text{energetic}} = \underbrace{\overline{\boldsymbol{\sigma}} : \overline{\boldsymbol{\varepsilon}}}_{\text{mechanical}} + \underbrace{\overline{\boldsymbol{\sigma}' : \boldsymbol{\varepsilon}'}}_{=0}. \tag{9}$$

It equates the average of a scalar product of stress $\boldsymbol{\sigma}$ and strain $\boldsymbol{\varepsilon}$ fields to the product of their averages $\bar{\cdot}$ [40]. Hazanot and Huez [41] show appropriate boundary conditions need to be applied in case of homogenisation over a finite domain B with boundary ∂B. These conditions commonly include [40]:

1. Uniform displacement $\boldsymbol{u}$ or Dirichlet boundary condition: $\boldsymbol{u}(\boldsymbol{s}) = \boldsymbol{\varepsilon}^0 \cdot \boldsymbol{s} \quad \forall \boldsymbol{s} \in \partial B$
2. Uniform traction $\boldsymbol{t}$ or Neumann boundary condition: $\boldsymbol{t}(\boldsymbol{s}) = \boldsymbol{\sigma}^0 \cdot \boldsymbol{n} \quad \forall \boldsymbol{s} \in \partial B$
3. Periodic boundary conditions: $\boldsymbol{u}(\boldsymbol{s}^+) = \boldsymbol{u}(\boldsymbol{s}^-) + \boldsymbol{\varepsilon}^0 \cdot (\boldsymbol{s}^+ - \boldsymbol{s}^-)\,,$ $\boldsymbol{t}(\boldsymbol{s}^+) = -\boldsymbol{t}(\boldsymbol{s}^-) \quad \forall \boldsymbol{s} \in \partial B$

Herein, $\boldsymbol{\varepsilon}^0$ and $\boldsymbol{\sigma}^0$ are uniformly applied strains and stresses, respectively, and $\boldsymbol{n}$ is the outward pointing normal vector on ∂B. Figure 5 shows a two-dimensional schematic of the resulting deformation for different boundary conditions. Six simulations with carefully applied boundary conditions then suffice to determine the 6×6 stiffness matrix $\boldsymbol{C}$ of a linear elastic material. A non-zero uniform strain (Dirichlet or periodic) ε^0_j results in $\overline{\sigma}_i = C_{ij}\varepsilon^0_j$, where $\overline{\sigma}_i$ is the volume averaged stress of component i. A non-zero uniform traction (Neumann) σ^0_j results in $\overline{\varepsilon}_i = S_{ij}\sigma^0_j$, where $\boldsymbol{S} = \boldsymbol{C}^{-1}$ and $\overline{\varepsilon}_i$ is the volume averaged strain of component i.

Figure 6 shows C_{11} values for 10 mesomodel realisations, homogenised using three different boundary conditions. The Dirichlet and Neumann conditions clearly provide upper and lower bounds, as proven in literature [40]. Meanwhile, periodic boundary conditions, shown to accurately predict the in-situ material response [42], provide a good compromise and are therefore selected as representative homogenised properties.

The homogenized stiffness matrix of a representative random mesomodel presented in Figure 7 shows a nearly orthotropic material behaviour, except for the non-zero C_{15} and C_{16} entries. The large values of these coefficients are largely explained by truncation of the in-plane and out-of-plane misalignment fields over a finite domain, generally leading to a non-zero mean misalignment of the meso-model. Orthotropy is restored by subtracting the mean value, $\mu(\theta_i) = \sum_{i=0}^{N} \theta_i / N$, from the mesomodel realisation. After homogenisation of the (now) orthotropic material behaviour, the mean misalignment should be reintroduced. This occurs at the macroscale as a variable which transforms the element. Table 3 shows that this zero mean misalignment approach does not alter the elastic response of a macroscale element. The anisotropic method retains the non-zero mean in the mesomodel realisation, while the orthotropic method first subtracts this non-zero mean value from the mesomodel and then reintroduces it on the macroscale.

3.2. Tensile strength prediction

The homogenized tensile failure strength equals the maximum volume averaged stress $\overline{\sigma}^{max}_{11}$ which a mesomodel can attain before failure. For example, initially, an increasing uniform traction load, leads to a proportional increase of $\overline{\sigma}_{11}$. Elements start failing after a while, decreasing the overall stiffness and transmitting extra load to the remaining elements until catastrophic failure occurs.

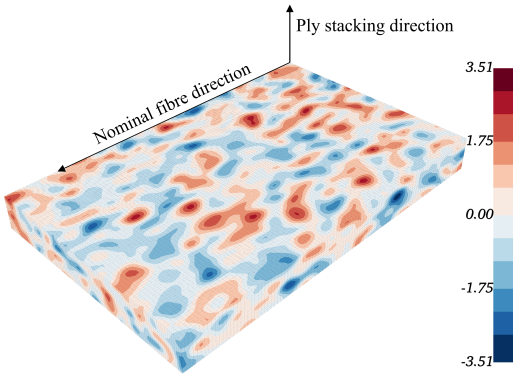

(a) Out-of-plane misalignment [°]

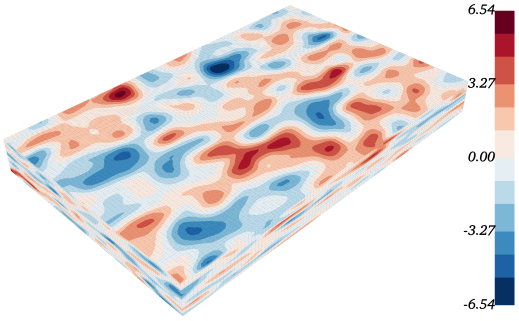

(b) In-plane misalignment [°]

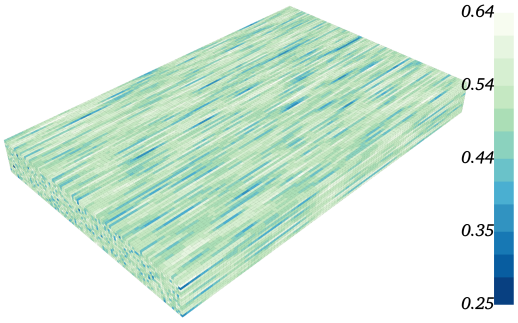

(c) Fibre volume fraction [-]

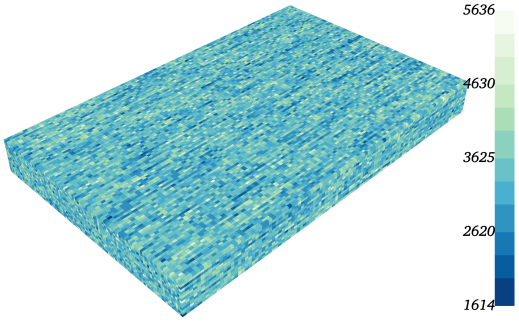

(d) Longitudinal tensile strength σ_{11} [MPa]

Figure 3: Example random field realisations on a unidirectional composite sample, with dimensions $11 \times 7 \times 1.05$ mm.

	C_{11}	C_{12}	C_{13}	C_{22}	C_{23}	C_{33}	C_{15}	C_{16}
Anisotropic [GPa]	118.942	2.8492	2.7243	7.9862	3.1929	7.9859	0.31069	−1.2551
Orthotropic [GPa]	118.947	2.8494	2.7243	7.9862	3.1929	7.9859	0.31133	−1.2633
$\frac{A-O}{A}$ [%]	–	–	–	–	–	–	−0.21	−0.66

Table 3: Comparison between non-zero and zero mean misalignment homogenization approaches.

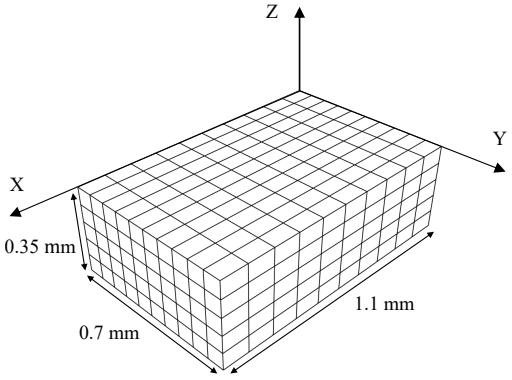

Figure 4: Schematic of the finite element mesomodel.

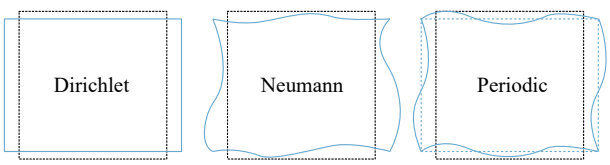

Figure 5: Deformation of body B for different boundary conditions.

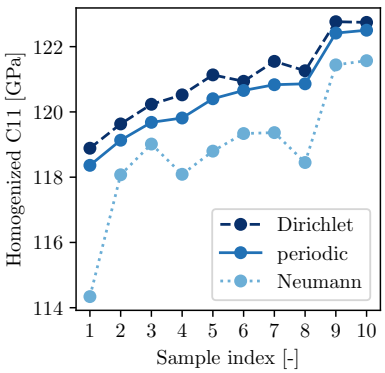

Figure 6: Comparison of 10 homogenized C_{11} values, sorted based on the periodic values in ascending order.

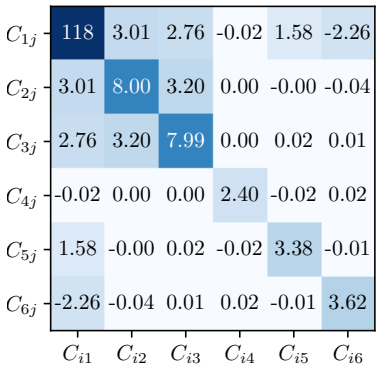

Figure 7: Homogenized stiffness matrix with periodic boundary conditions showing nonzero C_{15} and C_{16} entries.

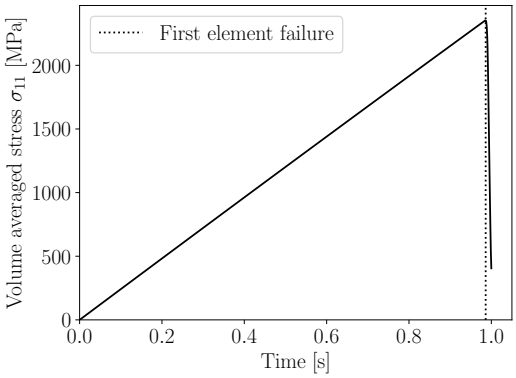

Figure 8: Volume-averaged longitudinal stess σ_{11} across time for an arbitrary meso-scale sample, showing that structural failure occurs immediately after first element failure.

Boundary conditions introduce stress concentrations at the edges of the mesomodel. Therefore, the mesomodel is augmented with extra infinite strength elements along each cartesian direction. The augmented length along each direction corresponds to the largest correlation length in that same direction. To take macroscale boundary conditions into account, mesomodels corresponding to edge elements at the macroscale are not augmented at their free faces.

A progressive damage model [43] shows mesomodel failure is brittle (see Figure 8). Since it occurs immediately after first element failure, a linear simulation adequately predicts the model strength. The non-linear simulation reduces the longitudinal stiffness $E_{11}^{damaged} = E_{11}\left(1 - d_f\right)$ using the damage variable d_f, which equals

$$d_f = \begin{cases} 0 & \text{if } Y_{11} \leq Y_{11}^{lim+} \\ 1 & \text{if } Y_{11} > Y_{11}^{lim+} \end{cases}, \tag{10}$$

where Y_{11} is a thermodynamic force, derived from the strain energy density E_D as

$$Y_{11} = \frac{\partial E_D}{\partial d_f} = \frac{\sigma_{11}^2}{2\left(1 - d_f\right)^2 E_{11}}. \tag{11}$$

This equation calculates the energy threshold Y_{11}^{lim+} by substituting σ_{11} with the longitudinal composite strength.

3.3. Correlated material parameters

Figure 9 shows that the homogenized material properties are intercorrelated. Copulas provide an excellent tool for fitting such multivariate distributions. They handle the marginal distributions $F_i(x_i)$ and correlation structure separately, due to Sklar's theorem [44]

$$F(x_1, ..., x_n) = C\{F_1(x_1), ..., F_n(x_n)\}. \tag{12}$$

Derivation, using the chain rule, leads to an expression in terms of the *probability density functions* (PDF) $f_i(x_i)$,

$$\begin{aligned} f(x_1, ..., x_n) = c_{1\cdots n}\left\{F_1\left(x_1\right), ..., F_n\left(x_n\right)\right\} \\ \cdot f_1\left(x_1\right) \cdots f_n\left(x_n\right), \end{aligned} \tag{13}$$

where $c_{1\ldots n}$ is an n-dimensional copula density. That is, each multivariate distribution F can be written in terms of its marginals F_i and an n-dimensional copula C, that describes the correlation structure [45].

Finding suitable n-dimensional copulas is challenging and in practice mostly bivariate copulas exist. However, it is possible to decompose the joint density function into conditional densities, like

$$\begin{aligned} f(x_1, ..., x_n) = f_1\left(x_1\right) f\left(x_2|x_1\right) f\left(x_3|x_1, x_2\right) \\ \cdots f\left(x_n|x_1, ..., x_{n-1}\right). \end{aligned} \tag{14}$$

From Equation 13 it follows that for conditional densities

$$\begin{aligned} f\left(x_2|x_1\right) &= c_{21}\left\{F_2\left(x_2\right), F_1\left(x_1\right)\right\} f_2\left(x_2\right) \\ f\left(x_3|x_1, x_2\right) &= c_{32|1}\left\{F\left(x_3|x_1\right), F\left(x_2|x_1\right)\right\} f\left(x_3|x_1\right). \end{aligned} \tag{15}$$

Therefore, it is possible to rewrite Equation 13 in terms of bivariate copulas. The same multivariate distribution, however, can be decomposed in multiple ways. As proposed by Bedford and Cooke [46, 47], vines provide a way of ordering these different decompositions, leading to the concept of vine copulas.

Fitting the right vine copula to a given multivariate distribution requires an heuristic algorithm due to a generally large number of parametrizations. The algorithm proposed by Dißmann et al. [48] is used because of its straightforward implementation using the Python package "pyvinecopulib" [49], and its good performance [50]. The algorithm sequentially identifies the whole vine. Maximization of the absolute empirical Kendall's τ ensures a reasonably well fitted decomposition into bivariate copulas. Meanwhile, selection of individual copulas occurs with the *Akaike information criterion* (AIC) in order to balance model simplicity with goodness of fit [50].

The marginal distributions are fitted by minimizing the negative log-likelihood function for the candidate distributions. The *Kolmogorov-Smirnov* (KS) test subsequently compares different candidates by calculating their p-value. If these results are inconclusive, either the simplest or, in

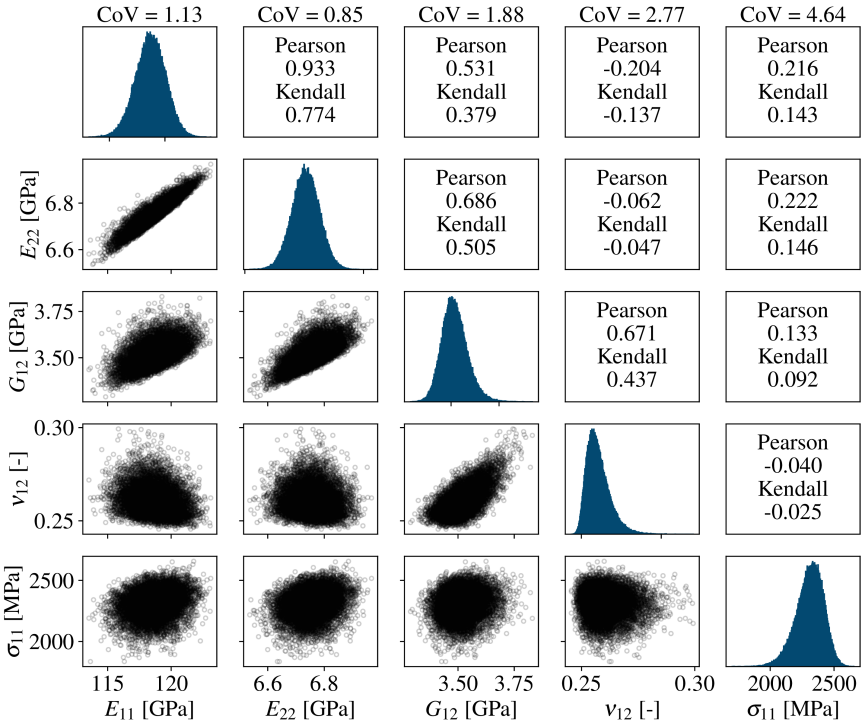

Figure 9: Correlation plot for 100,000 homogenized samples. The strength σ_{11} corresponds to the strength of a fully embedded mesoscale model.

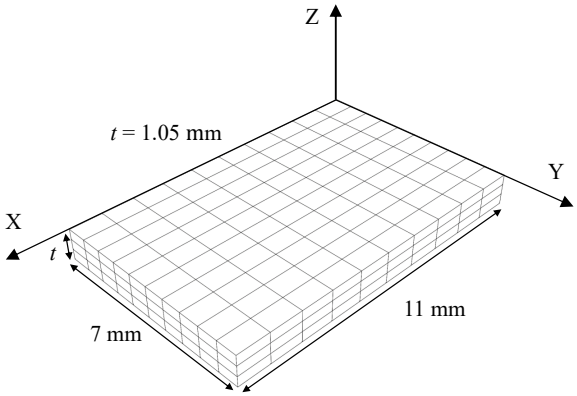

Figure 10: Indirect coupon model used for verification. It consists of $10 \times 10 \times 3$ elements.

case of physically bounded variables, a bounded distribution is preferred.

4. Results and discussion

The multiscale framework is illustrated on a unidirectional cuboid composite coupon. It is equal in size to $10 \times 10 \times 3$ mesomodels along the X, Y and Z axis, respectively. Therefore, a direct implementation of spatial variability on the coupon model remains computationally feasible. The coupon is simply constrained in a statically determinate manner, while a uniform traction is applied to both the $+X$ and $-X$ faces.

Coupon strength is predicted by two different models of the composite coupon. First, an "indirect" model, shown in Figure 10, uses the multiscale framework established earlier in order to reduce the number of elements at the macroscale (the coupon model). The model is meshed with linear hexahedral elements with a shape equal to the mesomodel. It indirectly accounts for spatial variability using intercorrelated material properties retrieved from homogenisation of a mesoscale model. Second, a "direct" model, similar to the indirect model except for a smaller mesh size, does not use the multiscale framework. Instead, it directly accounts for spatial variability at the macroscale. The model is also meshed with linear hexahedral elements with a shape equal to that of the elements of the mesomodel. The indirect model uses 300 elements at the macroscale, while the direct model requires 150,000 elements, which constitutes a 500 times increase. This highlights the computational efficiency of the indirect model. To estimate the coupon strength, 100,000 and 1000 stochastic realisations are sampled, respectively.

Figure 11 shows a comparison of the predicted coupon strength. This corresponds to the traction load at which the first element fails. Visual comparison of the direct and indirect model distribution shows that the empirical averages μ almost coincide (1919.9 MPa and 1924.3 MPa for the indirect and direct model, respectively). This is a significant improvement compared with previous results [23], where the effect of macroscale boundary conditions on the mesoscale homogenisation was not accounted for. However, the indirect model distribution appears more spread

out, as reflected in the higher coefficient of variance (3.55% compared to the direct model's 3.14%).

Two possible explanations can be mentioned. First, the mesomodel X, Y and Z lengths correspond to the largest correlation length along the same axis. This correlation length defines the distance for which the autocorrelation function drops below 0.1. Therefore, a non-negligible correlation remains beyond the boundaries of the mesomodel which is not taken into account by the indirect model. A second explanation may be the finite sample size of both the direct and indirect model. As a result, the empirical distributions contain a sampling error.

The first hypothesis is tested by creating an adjusted indirect model. The mesomodel is twice as large as the previous one, except for the Z- (thickness) direction. As shown by Figure 11 the resulting empirical distribution's shape matches more closely that of the direct model. In addition, the CoV reduces (3.55% to 3.38%) compared to the non-adjusted indirect model.

Testing of the second hypothesis is performed, first, using the two-sample Kolmogorov-Smirnov test. This test rejects the null hypothesis ($p < 0.05$) that the direct and indirect model's empirical strength distribution are drawn from the same distribution with a p-value equalling $p = 0.014$. Meanwhile, the p-value for the adjusted indirect model equals $p = 0.184$, indicating that it corresponds much more closely to the direct model distribution.

The second hypothesis is tested further by fitting each model's distribution to an analytical PDF. Afterwards, this analytical distribution is sampled in batches equal to the sample size a large number of times ($N = 10,000$). As such, the scatter on the empirical mean and standard deviation (STD) can be studied. As Table 4 shows, the limited number of samples for the direct model results in a relatively large scatter of μ and σ, with the mean of the adjusted indirect model laying within 2σ of the direct model's mean value. It further shows that the standard deviation of the adjusted indirect model decreases considerably compared to that of the non-adjusted indirect model.

Modelling method	Direct	Indirect	Adj. indirect
Mean μ [MPa]	1924.3	1919.9	1921.7
STD μ [MPa]	1.94	0.21	0.21
Mean σ [MPa]	60.5	68.2	64.9
STD σ [MPa]	1.70	0.21	0.20

Table 4: Scatter on indirect and direct model distributions due to finite sample size.

Table 5 shows the influence of individual types of imperfections on the homogenized material properties σ_{11} and E_{11}. Here, σ_{11} is the homogenized failure strength for a fully embedded mesomodel. These results are retrieved by sampling mesomodels ($N = 100,000$) and including only a subset of all the imperfections. The table shows that both the fibre misalignment and fibre volume fraction have a significant effect on the stochasticity of the homogenized properties. For example, the mean strength decreases by $\approx 1.5\%$ and the standard deviation increases by $\approx 7.2\%$.

	Strength σ_{11} [MPa]		Stiffness E_{11} [GPa]	
Included	μ	σ	μ	σ
V_f, θ_i, σ_{11}^f	2308.8	107.0	118.7	1.34
V_f, σ_{11}^f	2335.3	104.9	120.3	1.30
θ_i, σ_{11}^f	2319.6	103.0	118.8	0.48
σ_{11}^f	2344.3	99.8	120.4	0.00

Table 5: Influence of individual imperfections on the homogenized material properties of a fully embedded mesomodel.

In addition, Figure 11 shows the predicted coupon failure strength in case only fibre strength variability is accounted for, named Hierarchical Scaling Law (HSL) in the figure. It shows that the inclusion of spatial variability of the fibre misalignment and volume fraction considerably impacts the coupon strength, irrespective of whether the indirect or direct model is considered.

Moreover, it is studied whether excluding intercorrelation of the homogenized properties in the indirect model results in a significant coupon strength prediction difference compared to including it. As shown previously in Figure 11, including intercorrelation results in a strength prediction with $\mu = 1920\,\text{MPa}$ and $\sigma = 68.1\,\text{MPa}$. Meanwhile, excluding intercorrelation results in a strength underprediction with $\mu = 1913\,\text{MPa}$ and $\sigma = 69.0\,\text{MPa}$. While statistically significant, the effect seems negligible compared to the overall strength stochasticity.

5. Conclusion

This paper propagates the effect of material imperfections effectively by using a multi-scale methodology. The mesoscale serves to include spatial variability of the fibre misalignment and fibre volume fraction. A fibre-break model introduces fibre strength variability at the same scale. FE homogenisation of this mesomodel combined with vine copula modelling further enables a computationally efficient inclusion of this spatial variability at the structural (macro) scale.

The methodology closely matches the predicted failure strength of a coupon model, compared with a direct inclusion of spatial variability on the macroscale. Respectively, both methods predict a mean strength of 1922 MPa and 1924 MPa, and a similar variance. The indirect coupon model contains 75 elements, while the direct model contains 150,000 elements, highlighting its computational efficiency. Compared with previous research [23] the prediction improves considerably by the inclusion of macroscale boundary conditions during the FE homogenisation of the mesoscale model.

Propagation of only a subset of the three material imperfections shows that all have a considerable impact. The

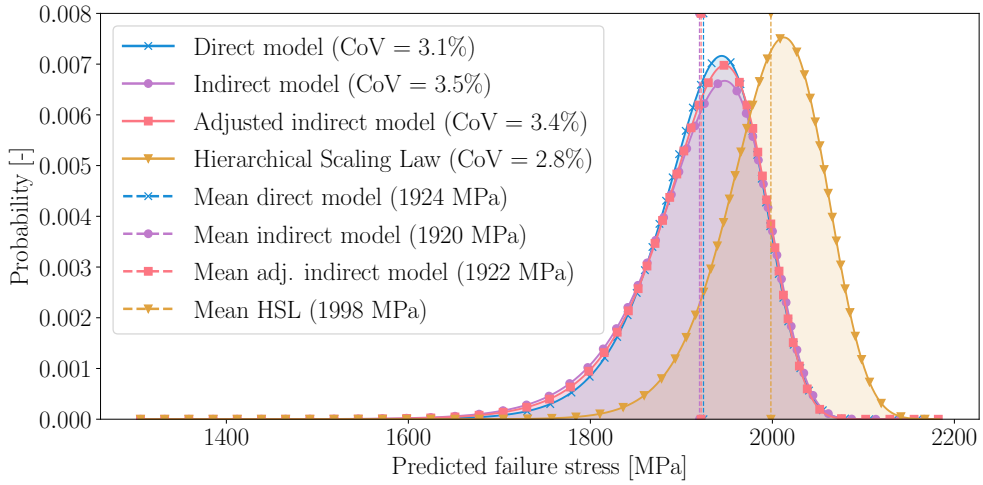

Figure 11: Predicted failure stress PDFs for different methodologies.

homogenized strength of a fully embedded mesomodel decreases by about 1.5% from 2344.3 MPa when simply including fibre strength variability, to 2308.8 MPa when also including fibre misalignment and volume fraction variability. Similarly, the standard deviation increases by approximately 7.2% from 99.8 MPa to 107.0 MPa.

A remaining challenge consists of the large number of mesomodel samples required to characterize the homogenized properties' distributions and correlation structure. Metamodelling provides a possible solution to this problem, by circumventing the relatively expensive finite elements simulations. In addition, the methodology is for now restricted to cuboid macroscale elements. An extension of the homogenisation procedure to tetrahedrally shaped elements, for instance, provides more flexibility for composite structure shapes at the macroscale.

CRediT authorship contribution statement

Ben Van Bavel: Conceptualization, Methodology, Software, Formal analysis, Writing - original draft. **Yinglun Zhao**: Data curation, Writing - review & editing. **Matthias Faes**: Conceptualization, Writing - review & editing. **Dirk Vandepitte**: Conceptualization, Writing - review & editing, Supervision. **David Moens**: Conceptualization, Writing - review & editing, Supervision.

Declaration of Competing Interest

The authors declare that they have no known competing financial interests or personal relationships that could have appeared to influence the work reported in this paper.

Acknowledgments

The work leading to this publication has been funded by the project "OptiVaS", which fits in the NANOFORCE research program, funded by SIM (Strategic Initiative Materials in Flanders) and VLAIO (Flanders Innovation & Entrepreneurship Agency).

References

[1] Y. Sugimoto, M. Shioya, K. Kageyama, Determination of intrinsic strength of carbon fibers, Carbon 100 (2016) 208–213. doi:https://doi.org/10.1016/j.carbon.2016.01.021.
URL https://www.sciencedirect.com/science/article/pii/S0008622316300215

[2] A. Bunsell, L. Gorbatikh, H. Morton, S. Pimenta, I. Sinclair, M. Spearing, Y. Swolfs, A. Thionnet, Benchmarking of strength models for unidirectional composites under longitudinal tension, Composites. Part A, Applied science and manufacturing 111 (2018) 138–150.

[3] F. Islam, S. Joannès, S. Bucknell, Y. Leray, A. Bunsell, L. Laiarinandrasana, Investigation of tensile strength and dimensional variation of t700 carbon fibres using an improved experimental setup, Journal of reinforced plastics and composites 39 (3-4) (2020) 144–162.

[4] L. Varandas, G. Catalanotti, A. Melro, R. Tavares, B. Falzon, Micromechanical modelling of the longitudinal compressive and tensile failure of unidirectional composites: The effect of fibre misalignment introduced via a stochastic process, International journal of solids and structures 203 (2020) 157–176.

[5] X.-Y. Zhou, P. Gosling, Influence of stochastic variations in manufacturing defects on the mechanical performance of textile composites, Composite structures 194 (2018) 226–239.

[6] F. Malgioglio, S. Pimenta, A. Matveeva, L. Farkas, W. Desmet, S. V. Lomov, Y. Swolfs, Microscale material variability and its effect on longitudinal tensile failure of unidirectional carbon fibre composites, Composite structures 261 (2021) 113300.

[7] M. Mehdikhani, L. Gorbatikh, I. Verpoest, S. V. Lomov, Voids in fiber-reinforced polymer composites: A review on their formation, characteristics, and effects on mechanical performance, Journal of Composite Materials 53 (12) (2019) 1579–1669.

[8] G. Stefanou, D. Savvas, M. Papadrakakis, Stochastic finite element analysis of composite structures based on mesoscale random fields of material properties, Computer methods in applied mechanics and engineering 326 (2017) 319–337.

[9] Y.-y. Wang, M. Lou, Y. Wang, W.-g. Wu, F. Yang, Stochastic failure analysis of reinforced thermoplastic pipes under axial loading and internal pressure, China Ocean Engineering 36 (4) (2022) 614 – 628. doi:10.1007/s13344-022-0054-3.
URL https://www.scopus.com/inward/record.uri?eid=2-s2.0-85139455173\&doi=10.1007

[10] M. Azizian, J. H. S. Almeida, Stochastic, probabilistic and reliability analyses of internally-pressurised filament wound composite tubes using artificial neural network metamodels, Materials Today Communications 31 (2022) 103627. doi:https://doi.org/10.1016/j.mtcomm.2022.103627.
URL https://www.sciencedirect.com/science/article/pii/S2352492822004913

[11] R. Rafiee, M. A. Torabi, Stochastic prediction of burst pressure in composite pressure vessels, Composite structures 185 (2018) 573–583.

[12] M. Chen, X. Zhang, K. Shen, G. Pan, Sparse polynomial chaos expansion for uncertainty quantification of composite cylindrical shell with geometrical and material uncertainty, Journal of marine science and engineering 10 (5) (2022) 670–.

[13] Y. Wang, M. Lou, Y. Wang, Stochastic analysis of failure pressure in reinforced thermoplastic pipes under axial loading and external pressure, Ocean Engineering 240 (2021) 109963. doi:https://doi.org/10.1016/j.oceaneng.2021.109963.
URL https://www.sciencedirect.com/science/article/pii/S0029801821013068

[14] B. Cai, Y. Liu, Z. Liu, X. Tian, R. Ji, Y. Zhang, Probabilistic analysis of composite pressure vessel for subsea blowout preventers, Engineering failure analysis 19 (1) (2012) 97–108.

[15] L. Solazzi, Stress variability in multilayer composite hydraulic cylinder, Composite structures 259 (2021) 113249.

[16] A. E. Burov, Burst pressure estimations of a composite pressure vessel accounting for the composite shell imperfections, Journal of Physics: Conference Series 1260 (11) (2019) 112007.

[17] R. Garcia-Martin, Álvaro Bautista-De Castro, L. J. Sánchez-Aparicio, J. G. Fueyo, D. Gonzalez-Aguilera, Combining digital image correlation and probabilistic approaches for the reliability analysis of composite pressure vessels, Archives of Civil and Mechanical Engineering 19 (1) (2019) 224–239. doi:https://doi.org/10.1016/j.acme.2018.10.001.
URL https://www.sciencedirect.com/science/article/pii/S1644966518301237

[18] B. Ellul, D. Camilleri, The influence of manufacturing variances on the progressive failure of filament wound cylindrical pressure vessels, Composite structures 133 (2015) 853–862.

[19] S. Camara, A. Bunsell, A. Thionnet, D. Allen, Determination of lifetime probabilities of carbon fibre composite plates and pressure vessels for hydrogen storage, International journal of hydrogen energy 36 (10) (2011) 6031–6038.

[20] J. P. B. R. Berro Ramírez, Wound composites damage modelling and characterization. application to burst prediction of hyperbaric wound composite pressure vessels (2013).

[21] M. P. Widjaja, M. Alves, M. Mavrogordato, S. Joannès, A. R. Bunsell, G. Mair, A. Thionnet, Effect of the Time Dependent Loading of Type IV Cylinders using a Multiscale Model, in: ICSH 2019 - 8th International Conference on Hydrogen Safety, Adelaide, Australia, 2019.
URL https://hal.archives-ouvertes.fr/hal-02315016

[22] B. Gentilleau, S. Villalonga, F. Nony, H. Galiano, A probabilistic damage behavior law for composite material dedicated to composite pressure vessel, International journal of hydrogen energy 40 (38) (2015) 13160–13164.

[23] B. Van Bavel, Y. Zhao, D. Vandepitte, D. Moens, M. Faes, Bridging the composite meso-macro gap: A numerically efficient spatial uncertainty quantification approach, in: Proceedings of USD2022, International Conference on Uncertainty in Structural Dynamics, 2022, pp. 4761–4777.

[24] F. Mesquita, S. Bucknell, Y. Leray, S. V. Lomov, Y. Swolfs, Single carbon and glass fibre properties characterised using large data sets obtained through automated single fibre tensile testing, Composites. Part A, Applied science and manufacturing 145 (2021) 106389.

[25] S. H. R. Sanei, R. S. Fertig, Uncorrelated volume element for stochastic modeling of microstructures based on local fiber volume fraction variation, Composites science and technology 117 (2015) 191–198.

[26] M. Sutcliffe, S. Lemanski, A. Scott, Measurement of fibre waviness in industrial composite components, Composites science and technology 72 (16) (2012) 2016–2023.

[27] Huntsman Corporation, Araldite® LY 1564 / Araldur® 917 / Accelerator 960-1 Data Sheet (2012).
URL https://farix.hu/pdf/1389709673.pdf

[28] Toray Industries, Inc., Torayca T700S Data Sheet - Rev. 3 (2018).
URL https://www.toraycma.com/wp-content/uploads/T700S-Technical-Data-Sheet-1.pdf.pdf

[29] A. Kaddour, M. Hinton, P. Smith, S. Li, Mechanical properties and details of composite laminates for the test cases used in the third world-wide failure exercise, Journal of composite materials 47 (20-21) (2013) 2427–2442.

[30] C.-C. Li, A. Der Kiureghian, Optimal discretization of random fields, Journal of engineering mechanics 119 (6) (1993) 1136–1154.

[31] M. G. Faes, M. Broggi, P. D. Spanos, M. Beer, Elucidating appealing features of differentiable auto-correlation functions: A study on the modified exponential kernel, Probabilistic Engineering Mechanics 69 (2022) 103269. doi:https://doi.org/10.1016/j.probengmech.2022.103269.
URL https://www.sciencedirect.com/science/article/pii/S026689202200042X

[32] H. Kim, M. D. Shields, Modeling strongly non-gaussian non-stationary stochastic processes using the iterative translation approximation method and karhunen–loève expansion, Computers & structures 161 (2015) 31–42.

[33] C. Creighton, M. Sutcliffe, T. Clyne, A multiple field image analysis procedure for characterisation of fibre alignment in composites, Composites. Part A, Applied science and manufacturing 32 (2) (2001) 221–229.

[34] Y. Swolfs, I. Verpoest, L. Gorbatikh, Hybridisation of self-reinforced composites: Modelling and verifying a novel hybrid concept (2015).

[35] S. G. Abaimov, A. A. Khudyakova, S. V. Lomov, On the closed form expression of the mori–tanaka theory prediction for the engineering constants of a unidirectional fiber-reinforced ply, Composite structures 142 (2016) 1–6.

[36] F. W. Zok, On weakest link theory and weibull statistics, Journal of the American Ceramic Society 100 (4) (2017) 1265–1268.

[37] A. Scott, M. Mavrogordato, P. Wright, I. Sinclair, S. Spearing, In situ fibre fracture measurement in carbon–epoxy laminates using high resolution computed tomography, Composites science and technology 71 (12) (2011) 1471–1477.

[38] S. Pimenta, A computationally-efficient hierarchical scaling law to predict damage accumulation in composite fibre-bundles, Composites science and technology 146 (2017) 210–225.

[39] R. Hill, Elastic properties of reinforced solids: Some theoretical principles, Journal of the mechanics and physics of solids 11 (5) (1963) 357–372.

[40] M. Ostoja-Starzewski, Material spatial randomness: From statistical to representative volume element, Probabilistic engineering mechanics 21 (2) (2006) 112–132.

[41] S. Hazanov, C. Huet, Order relationships for boundary conditions effect in heterogeneous bodies smaller than the representative volume, Journal of the mechanics and physics of solids 42 (12) (1994) 1995–2011.

[42] D. Pivovarov, R. Zabihyan, J. Mergheim, K. Willner, P. Steinmann, On periodic boundary conditions and ergodicity in computational homogenization of heterogeneous materials with random microstructure, Computer methods in applied mechanics and engineering 357 (2019) 112563.

[43] P. Ladevèze, D. Néron, H. Bainier, A Virtual Testing Approach for Laminated Composites Based on Micromechanics, Springer International Publishing, Cham, 2017, Ch. 23, pp. 667–698. doi:10.1007/978-3-319-46120-5_23.
URL https://doi.org/10.1007/978-3-319-46120-5_23

[44] M. Sklar, Fonctions de Répartition À N Dimensions Et Leurs Marges, Publications de l'Institut de Statistique de L'Université de Paris 8, 1959.

[45] K. Aas, C. Czado, A. Frigessi, H. Bakken, Pair-copula con-

structions of multiple dependence, Insurance, mathematics & economics 44 (2) (2009) 182–198.
[46] T. Bedford, R. M. Cooke, Probability density decomposition for conditionally dependent random variables modeled by vines, Annals of mathematics and artificial intelligence 32 (1) (2001) 245–268.
[47] T. Bedford, R. M. Cooke, Vines: A new graphical model for dependent random variables, The Annals of statistics 30 (4) (2002) 1031–1068.
[48] J. Dißmann, E. Brechmann, C. Czado, D. Kurowicka, Selecting and estimating regular vine copulae and application to financial returns, Computational statistics & data analysis 59 (1) (2013) 52–69.
[49] T. Nagler, T. Vatter, pycopulib: High performance algorithms for vine copula modeling (2021).
URL `https://pypi.org/project/pyvinecopulib/`
[50] C. Czado, Analyzing Dependent Data with Vine Copulas: A Practical Guide with R, Vol. 222 of Lecture notes in statistics, Springer International Publishing AG, Cham, 2019.